

The M_w 6.0 24 August 2014 South Napa Earthquake

by Thomas M. Brocher, Annemarie S. Baltay, Jeanne L. Hardebeck, Fred F. Pollitz, Jessica R. Murray, Andrea L. Llenos, David P. Schwartz, James Luke Blair, Daniel J. Ponti, James J. Lienkaemper, Victoria E. Langenheim, Timothy E. Dawson, Kenneth W. Hudnut, David R. Shelly, Douglas S. Dreger, John Boatwright, Brad T. Aagaard, David J. Wald, Richard M. Allen, William D. Barnhart, Keith L. Knudsen, Benjamin A. Brooks, and Katherine M. Scharer

INTRODUCTION

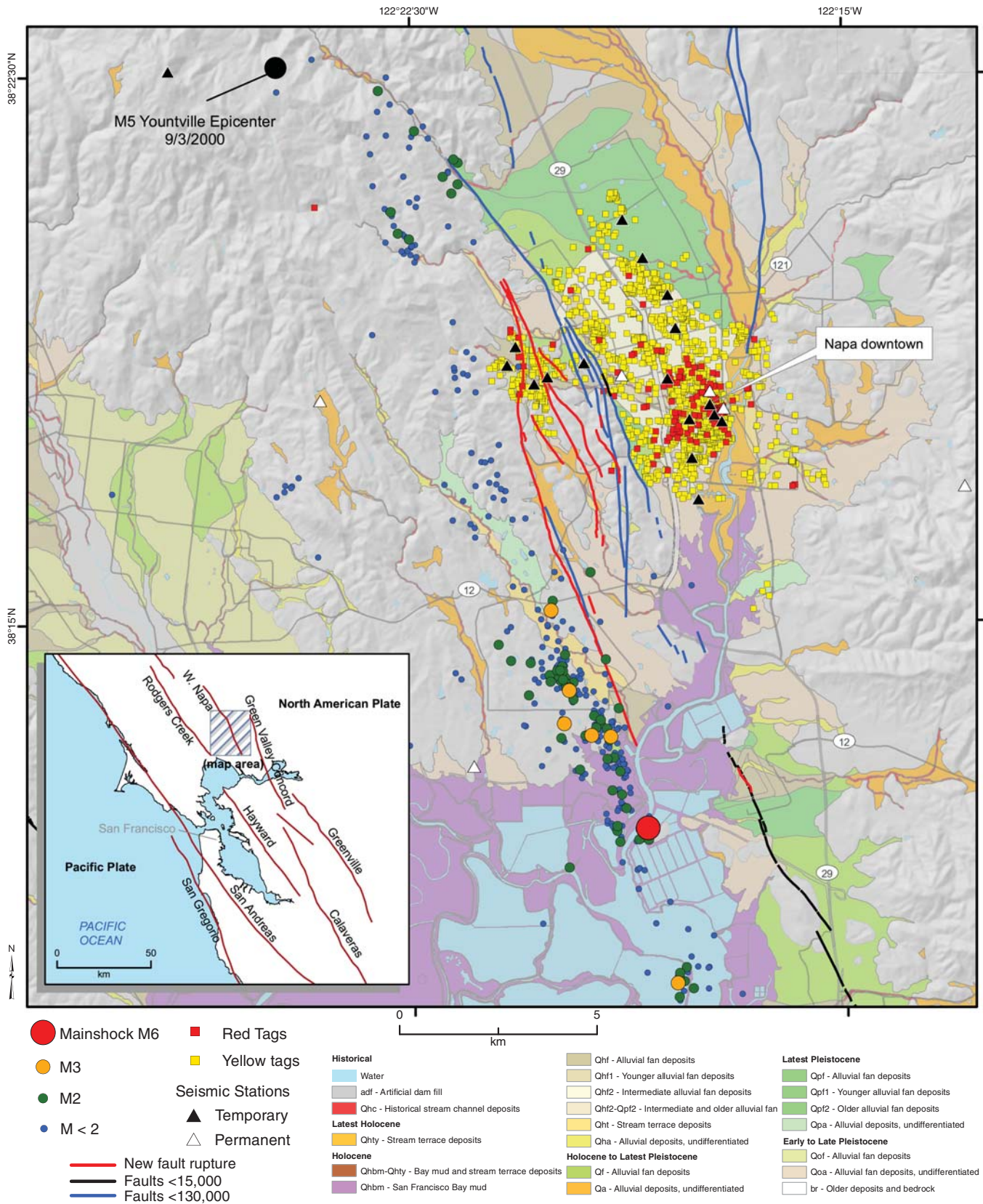
The M_w 6.0 South Napa earthquake, which occurred at 10:20 UTC 24 August 2014 was the largest earthquake to strike the greater San Francisco Bay area since the M_w 6.9 1989 Loma Prieta earthquake. The rupture from this right-lateral earthquake propagated mostly unilaterally to the north and up-dip, directing the strongest shaking toward the city of Napa, where peak ground accelerations (PGAs) between 45% g and 61% g were recorded and modified Mercalli intensities (MMIs) of VII–VIII were reported. Tectonic surface rupture with dextral slip of up to 46 cm was observed on a 12.5 km long segment, some of which was along a previously mapped strand of the West Napa fault system, although the rupture extended to the north of the mapped Quaternary strand. Modeling of seismic and geodetic data suggests an average coseismic slip of 50 cm, with a maximum slip of about 1 m at depths of 10–11 km. We observed up to 35 cm of afterslip along the surface trace in the week following the mainshock, primarily along the southern half of the surface rupture that experienced relatively little coseismic offset. Relocation of the sparse aftershock sequence suggests an echelon southwest- and northeast-dipping fault planes, reflective of the complex fault geometry in this region. The Napa basin and historic and late Holocene alluvial flood deposits in downtown Napa amplified the ground motions there. Few ground failures were mapped, reflecting the dry season (as well as a persistent drought that had lowered the groundwater table) and the short duration of strong shaking in the epicentral area.

TECTONIC SETTING OF THE SOUTH NAPA EARTHQUAKE

The South Napa fault rupture lies within an 80 km wide set of major north-northwest-trending faults of the San Andreas fault system, forming the boundary between the Pacific and

North American tectonic plates (Jennings, 1994; Fig. 1). The West Napa fault system is a relatively minor strike-slip fault in the Contra Costa shear zone, which transfers slip between the Northern Calaveras, West Napa, and Concord faults (Unruh and Kelson, 2002a,b; Kelson *et al.*, 2004, 2005; Wesling and Hanson, 2008; Brossy *et al.*, 2010). Block modeling of Global Positioning System (GPS) data estimated a slip rate of 4.0 ± 3.0 mm/yr on the West Napa fault (d'Alessio *et al.*, 2005). In the Uniform California Earthquake Rupture Forecast (UCERF 3) model, the entire Contra Costa shear zone was assigned a maximum slip rate of 1 mm/yr (Field *et al.*, 2013, appendix C, 18 pp). The earthquake was located near the eastern shore of San Pablo Bay, midway between two major active fault systems: the Hayward–Rodgers Creek fault system 12 km to the west and the Concord–Green Valley fault system 13 km to the east. The earthquake epicenter lies 1.7 km west of the main mapped surface trace of the West Napa fault system and close to the surface traces of the lesser known Carneros and Franklin faults (Graymer *et al.*, 2002). Although several faults are mapped in the vicinity of the earthquake, only the West Napa fault system is known to have displaced Holocene-age sediments (Wesling and Hanson, 2008).

The West Napa fault system forms the western margin of a basin that underlies much of Napa Valley. The basin, filled with Cenozoic sedimentary and volcanic deposits, is ~ 2 km deep beneath the city of Napa. The South Napa earthquake occurred where the prominent east-facing gravity and magnetic gradients associated with the main bedrock strand of the West Napa fault system diminish and are replaced by prominent west-facing gravity gradients that mark the eastern margin of the San Pablo Bay basin and the Carneros and Franklin faults (Langenheim *et al.*, 2006). The 2000 M_w 4.9 Yountville earthquake was attributed to the main bedrock strand of the West Napa fault system 20 km north-northwest of the South Napa epicenter (Langenheim *et al.*, 2006). Modeling of potential-field data, coupled with aftershock locations, indicates a



▲ **Figure 1.** Locations of the mainshock (red dot), aftershocks, surface ruptures (red lines), and locations of permanent (unfilled triangles) and temporary (filled triangles) seismic stations. Aftershocks are taken from [Hardebeck and Shelly \(2014\)](#). Locations of red- and yellow-tagged structures are from [Boatwright et al. \(2015\)](#). Surficial geology is from [Witter et al. \(2006\)](#). The inset map shows the location of the major strike-slip faults in the San Francisco Bay area.

steep southwest dip for the main bedrock strand at this location.

Historically, the M_w 7.8 1906 San Andreas fault earthquake and the M_w 6.3 1898 Mare Island earthquake both caused shaking in this region sufficient to seriously damage structures at Mare Island. The 1898 earthquake may have occurred about 20 km to the northwest of Mare Island on the southern Rodgers Creek fault (Toppozada *et al.*, 1981; Bakun, 1999), but analysis after the South Napa earthquake locates that earthquake closer to Mare Island (Hough, 2014). Although the 2000 M_w 4.9 Yountville earthquake ruptured the West Napa fault north of Napa, its energy was directed south toward Napa, where it produced damage.

SHAKEALERT EARTHQUAKE EARLY WARNING (EEW) PERFORMANCE

ShakeAlert, the prototype EEW system developed by the U.S. Geological Survey (USGS), University of California–Berkeley (UC Berkeley), Caltech, Eidgenössische Technische Hochschule (ETH), and the University of Washington, (Given *et al.*, 2014), successfully delivered an alert for the earthquake. The first ShakeAlert (based on ElarmS) used data from four stations, had an estimated magnitude of 5.7, and was issued 5.1 s after the earthquake originated. The locations and magnitudes of the earthquake provided by ShakeAlert were stable and remained accurate as an ever-increasing number of stations were included in the real-time analysis. The sending of the alert at 5.1 s after origin time provided prototype ShakeAlert users in Berkeley and San Francisco about 10 s of warning prior to the onset of the strongest shaking at those locations (intensity IV). With the available network geometry and communications, the blind zone of the ElarmS alert had a radius of about 16 km. The four stations that contributed to the first ElarmS alert all provided 1 s data packets, but the latency in transmitting data to the processing center ranged from 0.27 to 2.62 s. A denser seismic network and/or decreasing the latency in transmitting data to less than a second would have allowed alerts to be issued in less than 3 s for this event, reducing the blind zone to a radius of about 8 km and allowing an alert closer to the epicenter. The first EEW alert based on the onsite algorithm was issued 10.9 s after the earthquake origin time.

NEAR-REAL TIME EARTHQUAKE INFORMATION PRODUCTS

The first location, magnitude, focal mechanism, and ShakeMap (a map showing the shaking intensity; Wald, 2012), were reported 4 min after the origin time of the earthquake. The first ShakeCast, based on the ShakeMap and user-defined estimates of infrastructure fragility (Wald, 2012), was prepared for the California Department of Transportation 11 min after the earthquake. The first Prompt Assessment of Global Earthquakes for Response (PAGER) alert of probable fatalities and economic loss based on population exposure to the shaking (Wald, 2012) was produced 13 min after the origin time.

The ShakeMap was updated as additional strong-motion recordings were retrieved and incorporated, and the PAGER alert changed from yellow to orange to red, based on projected direct economic losses, which are reported to be on the order of one-half billion dollars (Earthquake Engineering Research Institute [EERI], 2014). All versions of PAGER estimated between 0 and 10 fatalities; one fatality was reported. These products are available at the USGS Event Summary page for this earthquake (see Data and Resources). Increased network density and/or faster data telemetry would have improved ShakeMap, ShakeCast, and PAGER performance.

The earthquake was widely felt in the San Francisco Bay area. The “Did You Feel It?” (DYFI) community intensity website received more than 41,000 entries, with the highest reported intensities (MMI VIII) in Napa. The earthquake was reported as felt by more than one respondent 300 km to the east in Reno, Nevada, 340 km to the north in McKinleyville, California, and 440 km south in Bakersfield, California. Geocoded DYFI entries show the highest intensities were reported north of the epicenter, which is consistent with directivity estimates for the earthquake, although intensities of VII were also reported in northern Vallejo. Because the Internet service to the most heavily impacted areas was down for an extended time, few DYFI reports were received from within the City of Napa.

CALIFORNIA EARTHQUAKE CLEARINGHOUSE

Within 12 hrs of the mainshock, and for the first time since the 1994 Northridge earthquake, the California Earthquake Clearinghouse opened a physical clearinghouse in a Caltrans facility located in Napa (EERI, 2014). The Clearinghouse is a cooperative organization in which any agency interested in postearthquake information is welcome to participate. In addition to the California Geological Survey (CGS), which serves as the permanent lead coordinating agency, the founding and managing partners of the Clearinghouse include the California Office of Emergency Services, the California Seismic Safety Commission, EERI, and the USGS. The California Department of Transportation, Caltrans, also provided a communications van that supported high-speed Internet connections. The Clearinghouse, which included Geographic Information Systems staff, provided logistics support to the field crews, assisted in obtaining overflights of the surface rupture, and coordinated the field surveys being made of the surface rupture and ground deformation. Morning and evening meetings were held to debrief the field crews. The Clearinghouse closed in the evening of 26 August.

MAINSHOCK LOCATION, MAGNITUDE, FOCAL MECHANISM, AND FINITE-FAULT INVERSION

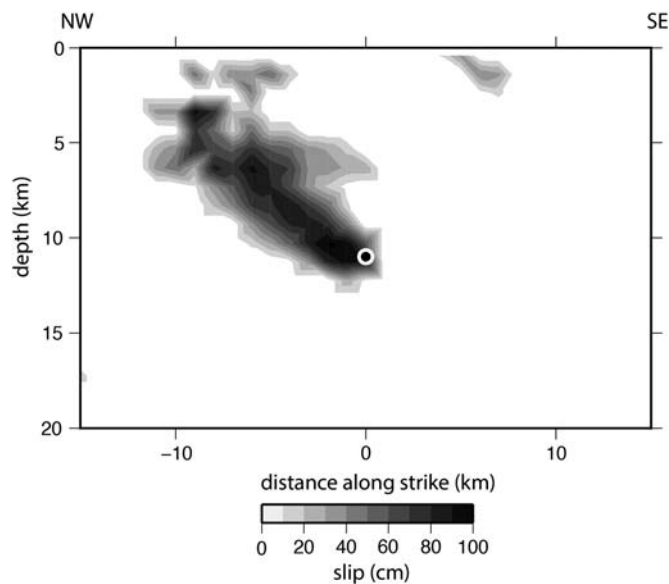
Initial estimates of the hypocenter of the M_w 6.0 (with a moment of 1.33×10^{18} N·m) earthquake, which occurred on 24 August 2014 at 10:20:44 UTC (3:20:44 local time), placed it about 8 km south-southwest of Napa at a depth of 11.3 ± 0.2 km. Although the relative depths have uncertain-

ties of a few hundred meters, the absolute depth uncertainties could be on the order of a few kilometers due to velocity model uncertainties. (Relocation of the event, described below, yields a revised depth of 9.4 km.) The hypocenter was located using 146 stations and 161 phases with an azimuthal gap of 29°. The distance to the nearest station was 4.0 km (Fig. 1), resulting in locations having reasonable depth control for the mainshock and its aftershocks.

Focal mechanisms are consistent with right-lateral motion along a plane striking 165°, dipping 85° to the southwest. This plane is compatible with the observed tectonic surface rupture. Moment tensor solutions by UC Berkeley also show right-lateral motion along a plane having nearly an identical strike, 157° or 158°, with a rake of 172°.

A preliminary slip model for the earthquake, based on seismic data, shows the rupture propagated mostly north-northwest and up-dip (Fig. 2). Slips at depth averaged about 50 cm in the elongated slip patch, with a maximum of about 1 m at depths of 10–11 km. This northward rupture propagation would have directed seismic energy toward Napa and produced the intensity distribution reported by DYFI.

Coulomb stress transfer models calculated for the earthquake using *Coulomb 3.4* (<http://usgsprojects.org/coulomb/>; last accessed February 2015) were consistent with a clear seismicity rate increase north of the mainshock and a modest increase south of the mainshock, roughly along the West Napa fault, where the stress is calculated to have increased by ~0.5 bar (Parsons *et al.*, 2014). Other small earthquakes occurred on or near the Green Valley fault, where the Coulomb stress is calculated to have increased by ~0.25 bars, although this section of the Green Valley fault is very active as recorded instrumentally. Coulomb stress changes of >0.5 bar are often but



▲ **Figure 2.** Slip model resulting from the inversion of seismic broadband data recorded at six University of California–Berkeley seismic network stations. The white circle provides the location of the hypocenter.

not always associated with increases in the rate of earthquakes, whereas changes of <0.1 bar are probably not important for triggering aftershocks.

AFTERSHOCK SEQUENCE AND LOCATION

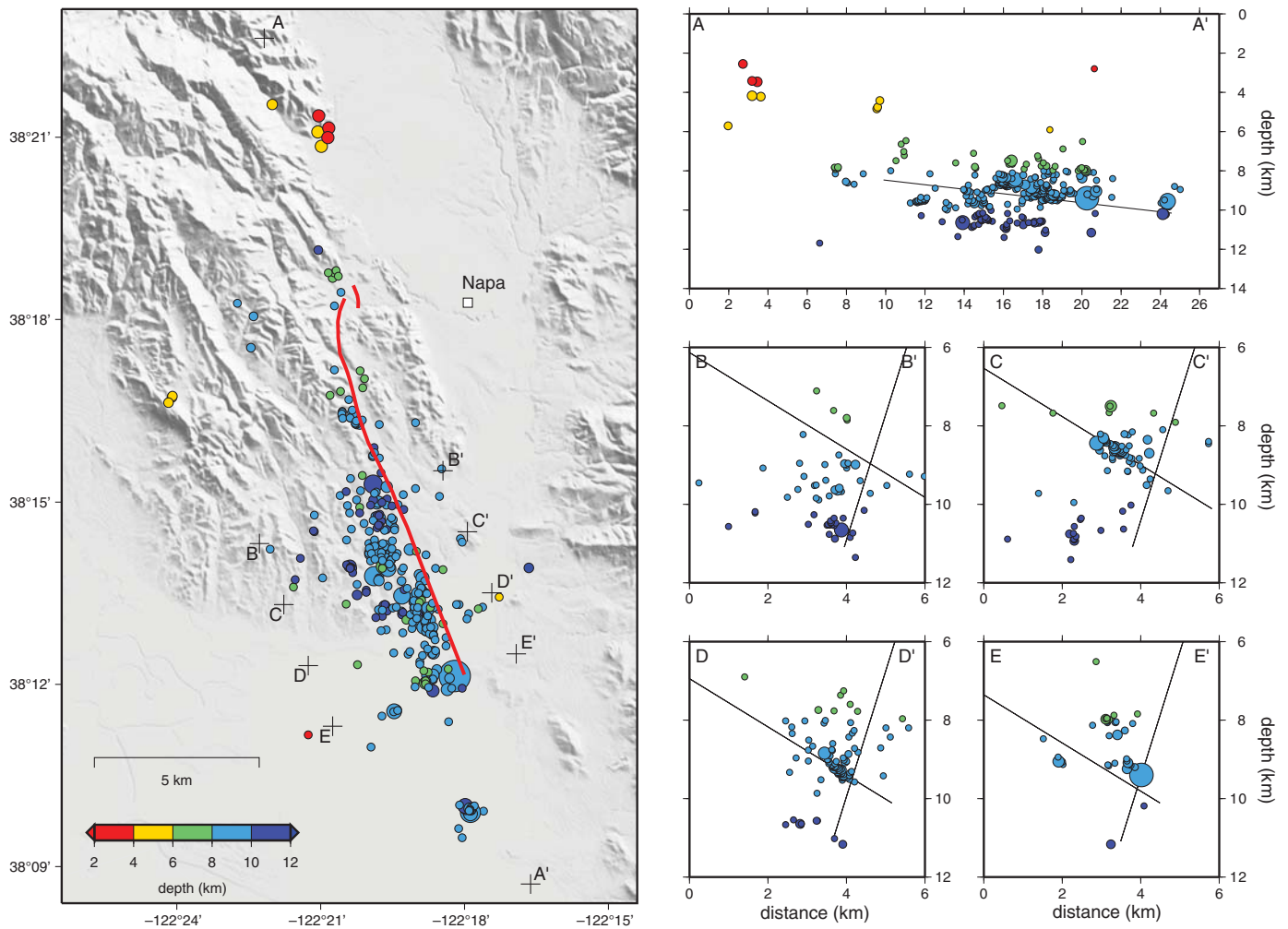
The aftershock sequence after one month (80 $M_w \geq 1.8$ aftershocks) was nearly four times less productive than for the 2004 M_w 6 Parkfield earthquake (320 $M_w \geq 1.8$ aftershocks). Both M_w 6 earthquakes, however, have b -values in the 0.7–0.8 range, similar to other northern California $M_w \sim 6$ aftershock sequences. Moreover, despite the relatively low aftershock productivity, the sequence is well described by epidemic-type aftershock sequence models (Ogata, 1988). The largest aftershock to date, an M_w 3.9 event, occurred just over two days after the mainshock. This aftershock was among the first to rupture south of the mainshock and triggered a cluster of its own aftershocks on the southern end of the West Napa fault (Fig. 1).

The first week of aftershocks were relocated using the *tomoDD* code (Zhang and Thurber, 2003) and the 3D seismic velocity model and station corrections of Hardebeck *et al.* (2007). Catalog P - and S -wave arrival times were used for relocation, as well as relative arrival times from waveform cross correlation. A matched filter approach was applied to identify aftershocks that do not appear in the network catalog.

We relocated all catalog earthquakes, and all matched-filter-detected events with at least eight waveform differential times having correlation coefficient ≥ 0.8 . We performed 20 iterations of *tomoDD*, the first 10 with the catalog times given more weight, and the last 10 with the waveform differential times given more weight. The relocated catalog consists of 375 hypocenters: 147 catalog aftershocks, 227 aftershocks detected by the matched filter approach, and the mainshock hypocenter. The relocated depth of the mainshock hypocenter is 9.4 km.

Although the surface rupture of the mainshock was well expressed, the fault plane of the mainshock is not well defined by the aftershocks. Most of the aftershocks occur between 8 and 11 km depth and form a diffuse ~10 km long north-northwest-trending feature to the north-northwest of the mainshock hypocenter (Fig. 3). In cross section, a sharply defined northeast-dipping seismicity plane is apparent north of the hypocenter, implying significant geometric complexity. In addition to the main aftershock zone, there are a few clusters of aftershocks to the northwest, close to but south-southeast of the Yountville earthquake and its aftershocks (Fig. 1), a cluster of aftershocks to the south of the mainshock, and a cluster of earthquakes in the Green Valley fault zone that is ~30 km directly to the east of the main aftershock zone.

To better understand the complex geometry of the aftershocks, the optimal anisotropic dynamic clustering (OADC) algorithm (Ouillon *et al.*, 2008) was used to identify the simplest planar fault geometry that fits the events of the main aftershock zone. Aftershock locations were fit to within the uncertainty, assumed here to be 0.5 km for all events. To account for sensitivity to randomness in the OADC procedure, we ran OADC 3000 times and use the suite of results to



▲ **Figure 3.** Relocated hypocenters of the first week of the South Napa earthquake sequence and the fault planes fit to the relocations. (Left) Map view with shaded topography. Symbol size represents earthquake magnitude, and fill color represents depth. Crosses and letters A–E indicate cross-section end points. The red lines show the approximate location of the mapped surface rupture. (A) Along-strike section. The black line indicates the intersection of the two optimal anisotropic dynamic clustering (OADC) planes. (B–E) Cross-section views of earthquakes within 1 km of the sections are shown. The black lines indicate the position of the two OADC planes at the location of the cross section.

identify stable features and their uncertainty. The OADC algorithm returns two stable planes, which occur in 84% and 73% of the runs. No other plane occurs in more than 30% of the runs.

One of the OADC-determined planes corresponds to the northeast-dipping seismicity structure visible in cross section. This plane strikes $357^\circ \pm 25^\circ$ and dips $33^\circ \pm 24^\circ$ to the east. The other plane strikes $162^\circ \pm 9^\circ$ and dips $72^\circ \pm 19^\circ$ to the southwest. This structure is visible only as a diffuse zone of seismicity in some cross sections. This second plane is similar in orientation to the fault plane of the mainshock moment tensor, so it may represent aftershocks occurring in the area around the mainshock rupture. The occurrence of most aftershocks to the west of the mapped surface rupture is consistent with the southwest dip of the mainshock fault plane.

The mainshock hypocenter and many of the aftershocks occur near the intersection of the two apparent fault planes. The plane intersection deepens to the south-southeast, due

to the difference in strike, corresponding to a slight deepening of the densest aftershock zone toward the south-southeast. The aftershock geometry suggests that stress is concentrated at the intersection of two active fault structures, encouraging nucleation of the mainshock and the majority of aftershocks. If this model is applied more broadly, it suggests that seismicity streaks reflect the linear intersection of planar faults. In previous earthquakes, seismicity streaks can persist over decades at least and are not reset by stress redistribution when a mainshock occurs (e.g., [Thurber et al., 2006](#)), also suggesting a link to fault geometry.

SPATIAL VARIABILITY OF STRONG-GROUND MOTIONS

PGAs of 45%g–61%g and peak ground velocities (PGVs) of 45–90 cm/s from the M_w 6.0 South Napa earthquake were

recorded in the Napa area, damaging many older buildings and resulting in more than 100 red-tagged structures (Boatwright *et al.*, 2015). The recorded data are of engineering interest as 9 strong-motion recordings were in excess of 30%g, 3 strong-motion recordings were made at epicentral distances less than 10 km, and 20 recordings were made at epicentral distances less than 20 km. The highest PGA (0.995%g) was recorded at Crockett beneath the Carquinez bridge: it is possible that the acceleration recorded there reflects a soil–structure interaction or an unusual path effect.

The recorded ground motions for PGA, PGV, and pseudospectral accelerations (PSA) at periods of 0.3, 1.0, and 3.0 s were compared with five ground-motion prediction equations (GMPEs), the four Next Generation Attenuation–West 2 GMPEs and that of Graizer and Kalkan (2015), to analyze both relative source and attenuation properties (see also Baltay and Boatwright, 2015). Overall, the GMPEs matched the median level of ground motion and the general distance decay, as well as the scatter in the data (Fig. 4). However, for most GMPEs at most periods, the attenuation in the data is stronger than that in the models, most obviously at the shorter periods (i.e., PGA). The DYFI data also indicate higher than average macroseismic intensities within 20 km of the epicenter and lower than average values at greater distances. This observation likely indicates the attenuation structure in the Napa and San Joaquin–Sacramento

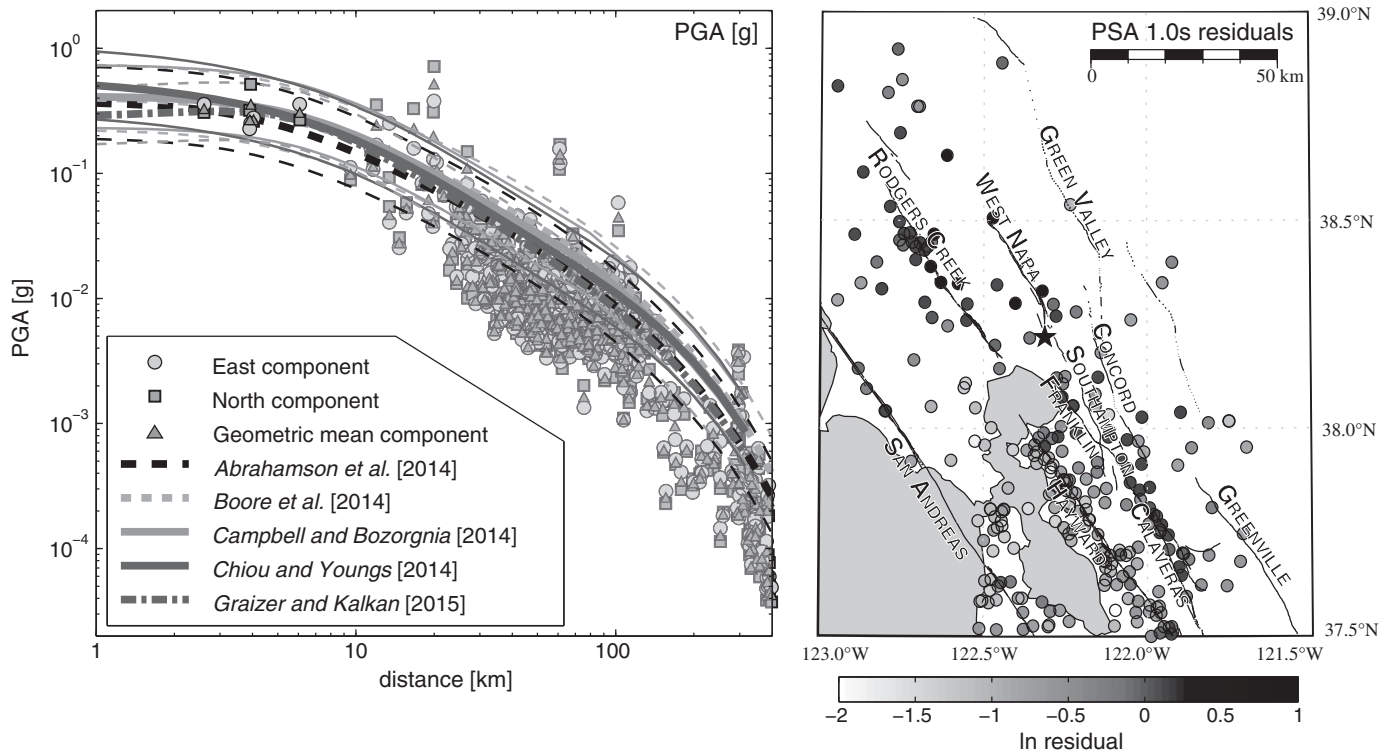
delta region is stronger than the average attenuation in California, on which the GMPEs were built.

At close distances, within ~20 km, the PGA data compare very well with the GMPEs (Fig. 4, left); because stress drop is most closely linked to PGA recordings at nearby stations, we infer the South Napa earthquake was of average stress drop, corresponding to ~5 MPa (Baltay and Hanks, 2014).

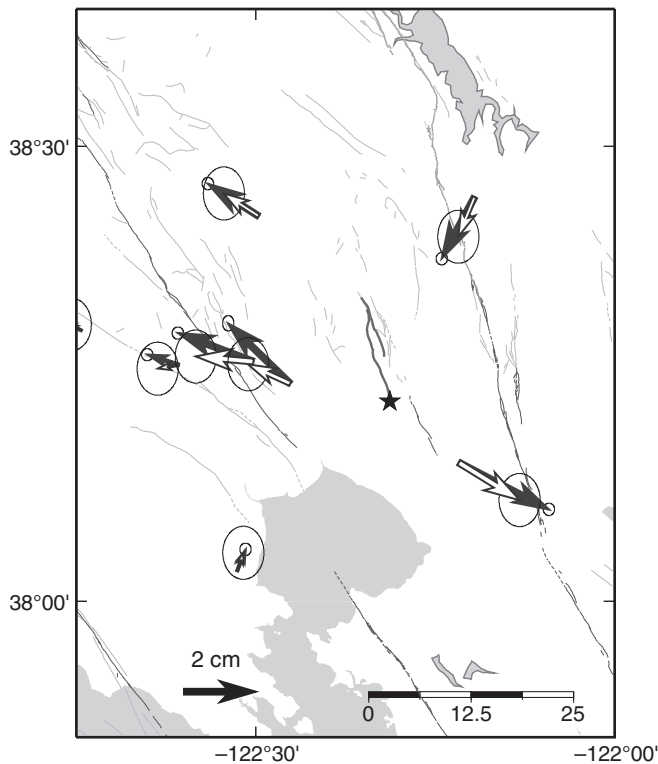
The residual maps show positive residuals (stronger than predicted ground motion) in the north along both the West Napa fault and in the Sonoma basin, likely due to the northerly rupture directivity, and along the Rodgers Creek fault, especially at the longer periods (e.g., Fig. 4, right, for PSA of 1.0 s). Particularly at 1.0 s, there also are strong positive residuals at stations to the south of the earthquake, showing a linear feature in the along-strike direction. These may align with a Quaternary-active fault near the Franklin or Southampton fault and continue south to the Calaveras fault. If so, they may be indicative of a fault-guided wave, indicating that these other structures may be thoroughgoing.

GEODETIC MODELS OF COSEISMIC SLIP AND AFTERSLIP

Time series from 64 regional continuous GPS (cGPS) sites and 13 campaign or survey-mode GPS (SGPS) stations reoccupied



▲ **Figure 4.** (left) Observed ground motion from the ShakeMap compared with five ground motion prediction equations (GMPEs): Abrahamson *et al.* (2014), Boore *et al.* (2014), Campbell and Bozorgnia (2014), Chiou and Youngs (2014), and Graizer and Kalkan (2015). Data are adjusted with the Seyhan and Stewart (2014) site correction to a $V_{S30} = 760$ m/s; the east and north components are shown separately, as along with their geometric mean. Median GMPEs and $\pm 1\sigma$ are shown, calculated for M_w 6.05 and for $V_{S30} = 760$ m/s, and a strike-slip focal mechanism with surface rupture. (right) Spatial residuals from the Abrahamson *et al.* (2014) GMPE for pseudospectral accelerations (PSA) of 1.0 s.



▲ **Figure 5.** Displacements differenced from pre-earthquake measurements at six continuous Global Positioning System (cGPS) sites using 5 min kinematic solutions (white vectors) and 24 hr solutions (black vectors). Error ellipses show 95% confidence. The mapped surface rupture is shown by the heavy gray curve, and the earthquake epicenter is indicated by the black star.

within three days of the earthquake constrain the coseismic displacement field at the Earth's surface. Comparison of the 5 min kinematic solutions from the cGPS stations (providing the most direct estimates of the coseismic offsets) with 24 hr solutions (Fig. 5) indicates that shallow displacements grew an additional 30%–50% during the first 24 hrs following the earthquake. This afterslip is best illustrated by horizontal-component time series for P261, the closest cGPS site to the West Napa fault (Fig. 6).

Coseismic offsets of a few centimeters were estimated from the GPS daily position time series for most of the cGPS and SGPS stations (Fig. 7). For each station, we fit a linear trend (interseismic motion), a coseismic step, and postearthquake Omori decay (with fixed time constant) using the approach of Langbein (2004), which accounts for temporally correlated noise; for cGPS sites, we also included seasonal terms. Using daily positions, combined with the time lag between the earthquake and initial campaign GPS measurements, resulted in the mapping of some postseismic displacement into the coseismic offset estimates. Consistent with its proximity to the fault plane, campaign site DEAL, located 770 m west of the trace of the surface rupture, moved about 23 cm to the north-northwest. This observation would suggest ~46 cm of total slip at the surface occurred in this location.

Interferometric Synthetic Aperture Radar (InSAR) data place additional constraint on the coseismic deformation. The earliest repeat pass was obtained on 27 August 2014 by the COSMO–SkyMed (CSK) 2 satellite, which repeated a pass on 26 July 2014. The unwrapped interferogram representing its range change from X-band Synthetic Aperture Radar (SAR), shown in Figure 8a, reveals a quadrant pattern of deformation consistent with a strike-slip rupture. Because the satellite orbit is descending looking to the west, positive range change is consistent with either uplift or eastward motion. As for the GPS data, this interferogram contains both coseismic motions and early afterslip.

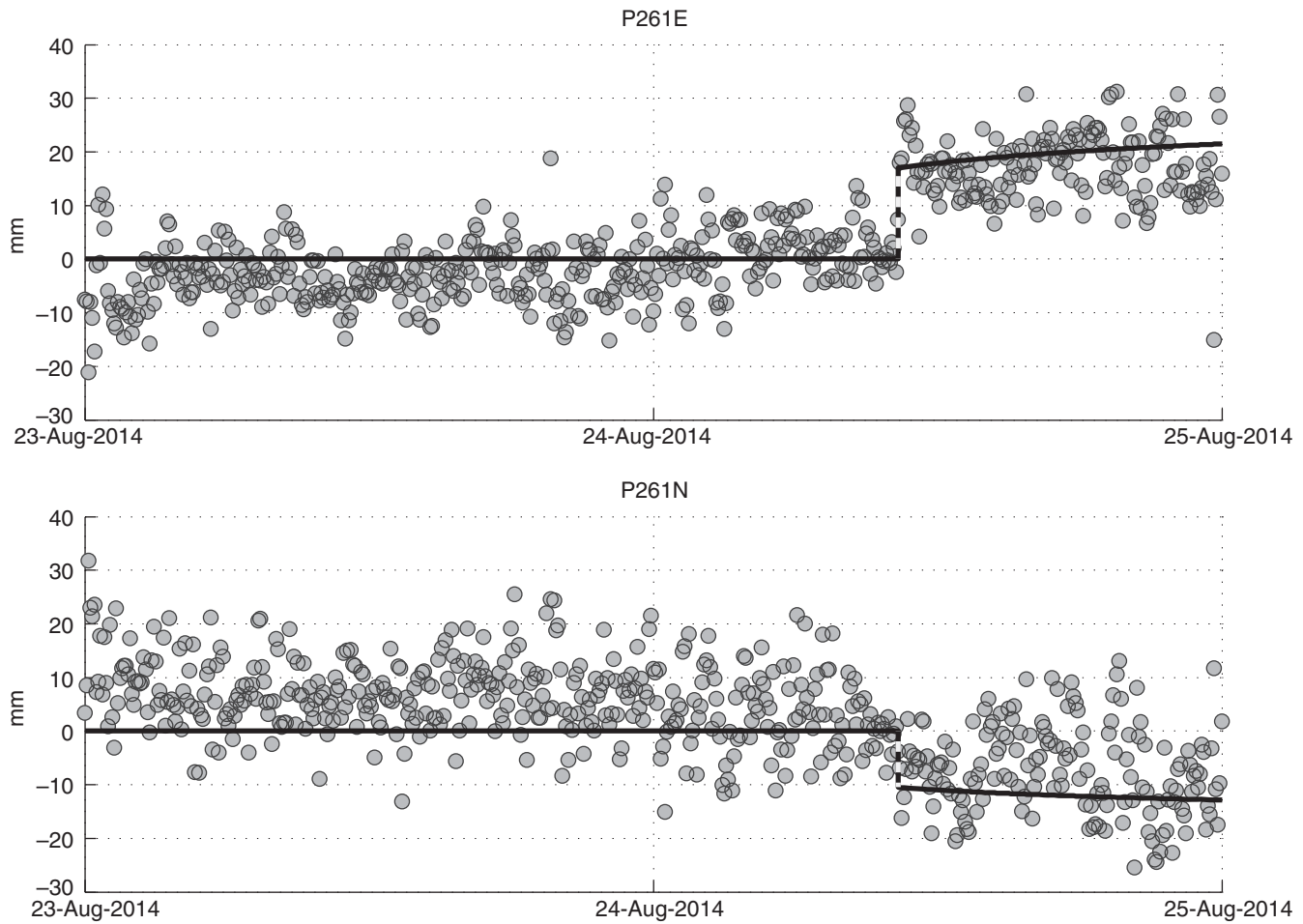
We inverted the GPS and InSAR data for slip distributions using the cascading adaptive transitional metropolis in parallel algorithm (Minson *et al.*, 2013). The model fault follows the western branch of the mapped surface rupture and is assumed to extend vertically to 12 km depth. We discretized the fault into subfaults that are ~1 km in down-dip dimension and 1.5 km in along-strike dimension. Strike slip was given a uniform prior distribution, that is, truncated at –5 mm to enforce positive (right lateral) motion. The dip-slip component was given a Gaussian prior distribution of 0 m with a standard deviation of 5 mm. We applied spatial averaging to the slip distribution below 1 km depth via a moving arithmetic mean with averaging lengths of three subfaults in the down-dip and along-strike direction.

Figure 9a shows the results of inverting the GPS offsets estimated from the daily position time series, along with coseismic surface rupture measurements (Brooks *et al.*, 2014; Ponti *et al.*, 2014; Trexler *et al.*, 2014), for the surface coseismic slip distribution. The surface slip (Fig. 10) and GPS data (Fig. 7) are fit reasonably well, and the majority of inferred slip underlies the region experiencing near-fault postseismic displacement. The slip distribution has an M_w 6.1, slightly larger than the M_w 6.0 inferred from seismic data, reflecting the inclusion of afterslip into the GPS offsets.

Figure 9b shows the results of jointly inverting the GPS and InSAR data. The fit to the data is shown in Figures 8b and 11. In these inversions, we use the approach of Johanson and Bürgmann (2010) to determine the relative weighting of GPS and InSAR data. The resulting slip distribution is somewhat complementary to that based solely on the GPS and surface slip data from 24 August, with slip extending deeper as well as in both directions along-strike from the area of inferred peak slip of 24 August. In comparison with the results in Figure 9a, additional moment release with equivalent M_w 5.5 occurred in the three days following the mainshock. The inversion results suggest that some afterslip may have occurred below 1 km depth on the northwest half of the fault.

SURFACE RUPTURE AND AFTERSLIP

The South Napa earthquake was the first earthquake in the San Francisco Bay area to produce a significant surface rupture since the 1906 San Francisco earthquake. The mapped surface rupture extended along and between mapped Quaternary and

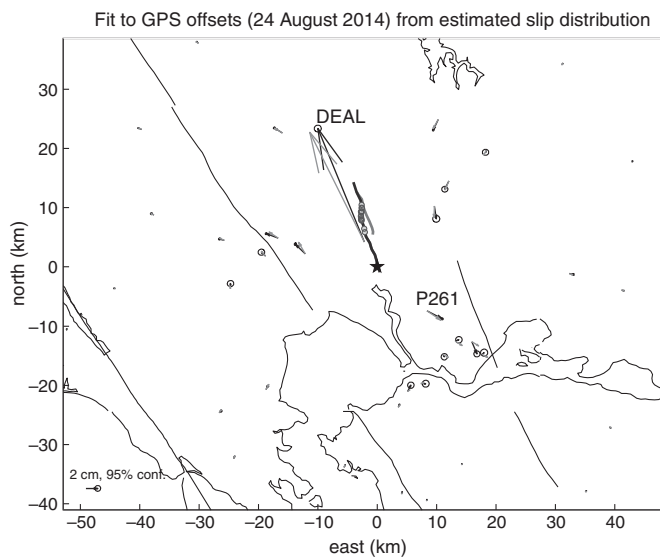


▲ **Figure 6.** East- and north-component kinematic time series at the Plate Boundary Observatory site P261 (see Fig. 7 for location). A slope proportional to the pre-earthquake velocity has been subtracted. The vertical dashed line segments indicate the coseismic offset, and the solid curves are flat pre-earthquake and follow an Omori decay postearthquake.

Holocene active strands of the West Napa fault (Fig. 1). The earthquake struck in a populated region containing a large number of well-maintained roads and vineyards, which facilitated mapping of the surface rupture. Field reconnaissance began within a few hours of the earthquake and included road surveys and helicopter overflights provided by the California Highway Patrol that were coordinated by the CGS–EERI Earthquake Clearinghouse. The mapped surface rupture consisted primarily of a zone of right-lateral fractures from less to a meter to more than tens of meters wide. Although the rupture varied along the fault, it was usually observed as a zone of echelon left-stepping fractures (Fig. 12). Field mapping was assisted by lineaments observed in SAR data, initially interferograms of Agenzia Spaziale Italiana’s CSK data (X-band), National Aeronautics and Space Administration/Jet Propulsion Laboratory’s Uninhabited Aerial Vehicle Synthetic Aperture Radar (UAVSAR) (L-band) data, and the European Space Agency’s (C-band) Sentinel-1-A data ([Geotechnical Extreme Events Reconnaissance \[GEER\], 2014](#)).

The mapped surface rupture extended ~12.5 km north-northwest from the town of Cuttings Wharf in the south

to north of Alston Park in the City of Napa (Fig. 13). A complex pattern of surface slip was observed along six different subparallel fault strands. Net surface slip was highest along fault strand A, which was also the longest fault strand that ruptured in the earthquake. A late Quaternary active strand of the West Napa fault had previously been mapped along the center section of strand A (Fig. 1). The maximum net surface slip along strand A, about 46 cm, was measured about 10 km north-northwest of the epicenter and is thought to be entirely coseismic. Strand C, located east of strand A, was the second longest surface fault rupture and had the second highest amount of surface slip, reaching a maximum of 8 cm in Brown’s Valley. Surface slip on the shorter strands B and D–F is also thought to be primarily coseismic and reached a maximum of 6 cm. Surface slip on strand F, on a Holocene active strand of the mapped West Napa fault at the Napa County Airport (Fig. 1), was minor. Surface slip on the other strands of the West Napa fault east of strand A could have resulted from either triggered slip or surface rupture ([Hudnut *et al.*, 2014](#)). The surface slip estimates shown on Figure 10 represent the earliest measurements made following the

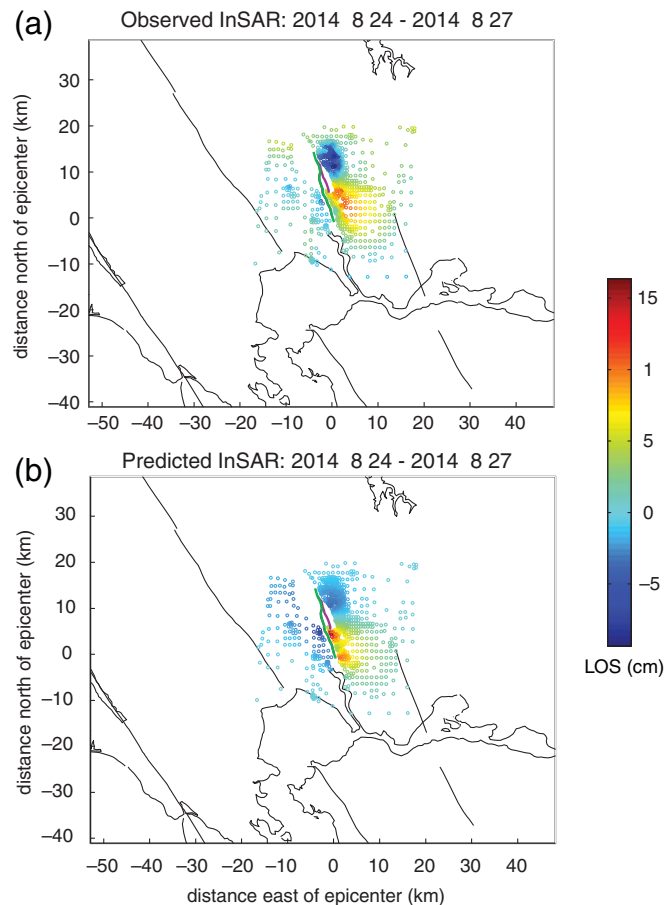


▲ **Figure 7.** Global Positioning System (GPS) offsets for 24 August 2014. Black arrows are estimated from the position time series; gray arrows are predicted from the slip model shown in Figure 9a. The dark gray curve shows the surface trace of the model fault, the light gray curve shows the location of the mapped eastern strand of surface rupture (not included in model), and the gray dots show locations of surface offset measurements from 24 August 2014.

earthquake. Nonetheless, some of these measurements may include afterslip.

Within the first 24 hrs following the earthquake, afterslip was observed from the ongoing development of surface cracking on roads and other man-made features. To better quantify the afterslip, the USGS established four alignment arrays across the fault (Lienkaemper *et al.*, 2014). Afterslip continues to accumulate more rapidly south of the maximum coseismic slip locality on strand A; it also accumulates to the north of the maximum coseismic slip location but at a much lower rate than was observed for the first 48 hrs following the mainshock (Hudnut *et al.*, 2014; Lienkaemper *et al.*, 2014). Up to 20 cm of right-lateral afterslip was observed within 48 hrs of the mainshock, mainly on the southern half of strand A. The ongoing analysis of imagery, repeat mobile Light Detection and Ranging (LiDAR) data, and campaign and continuous GPS data are expected to provide more information on the amount and location of afterslip along the rupture zone.

Comparison with 11 other moderate California strike-slip earthquakes since 1948 indicates that the South Napa earthquake coseismic surface rupture length and slip were unusually large (Table 1). Eleven other earthquakes, having comparable magnitudes between 5.5 and 6.15 (average M_w 5.9) and comparable focal depths between 5.8 and 14.8 km (average 9.4 km), had an average coseismic surface rupture length of 4.6 km and an average coseismic surface slip of 4.3 cm. Four of these earthquakes had no coseismic surface rupture, and six had coseismic surface slips of 1 cm or less. In contrast, the South Napa earth-

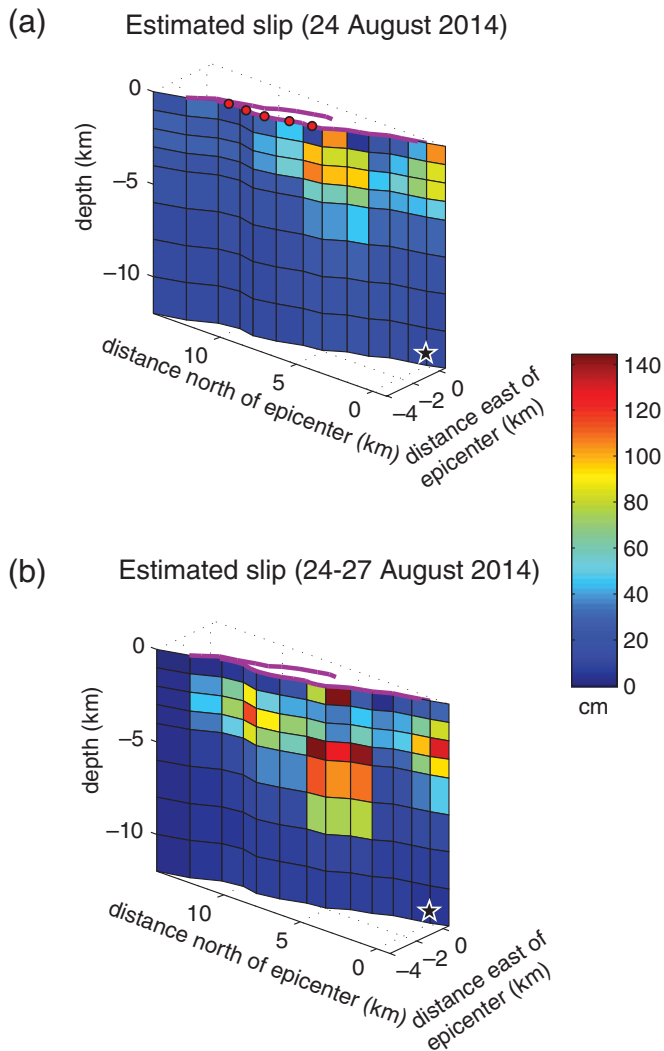


▲ **Figure 8.** COSMO-SkyMed interferograms spanning 26 July 2014–27 August 2014. The positive line-of-sight displacement corresponds to uplift and eastward movement. The heavy green curve shows the surface trace of the model fault, and the heavy purple curve shows location of mapped eastern strand of surface rupture.

quake produced a surface rupture length nearly three times larger than the average surface rupture length and a coseismic surface slip that is 14 times larger than the average slip. The observed surface afterslip for the South Napa earthquake, up to 35 cm, is also several times higher than the average of 5.1 cm.

PAUCITY OF GROUND FAILURE

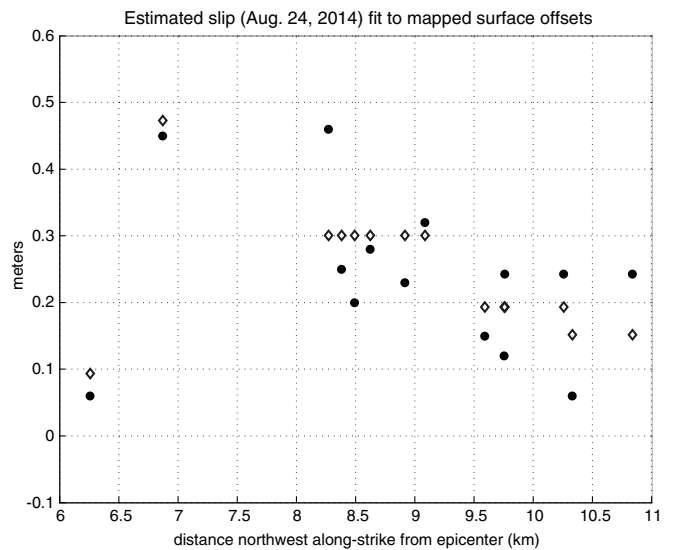
Few observations of liquefaction, landslides, or other ground failures were identified in reconnaissance surveys following the earthquake. Sand boils were noted in the Napa River channel in Napa at the Third Street Bridge (GEER, 2014). Some failures of road cuts and dislodged boulders were noted to the northwest of the epicenter (Walter Mooney, written comm., 2014). These findings are in accord with the compilation by Yound and Hoose (1978), which does not report ground failures in Napa Valley produced by historical earthquakes in northern California, including the 1892 Vacaville, 1898 Mare Island, and 1906 San Francisco earthquakes. Yound and Hoose



▲ **Figure 9.** Inferred slip distributions. (a) Slip on 24 August 2014, inferred from GPS and surface offset data. The star marks the hypocenter. Red dots mark subfaults, for which there are one or more surface rupture observations. The purple curve at the top of the fault marks the surface rupture from field mapping. (b) Slip from 24–27 August 2014 (inclusive of coseismic slip), inferred from GPS and Interferometric Synthetic Aperture Radar (InSAR) data.

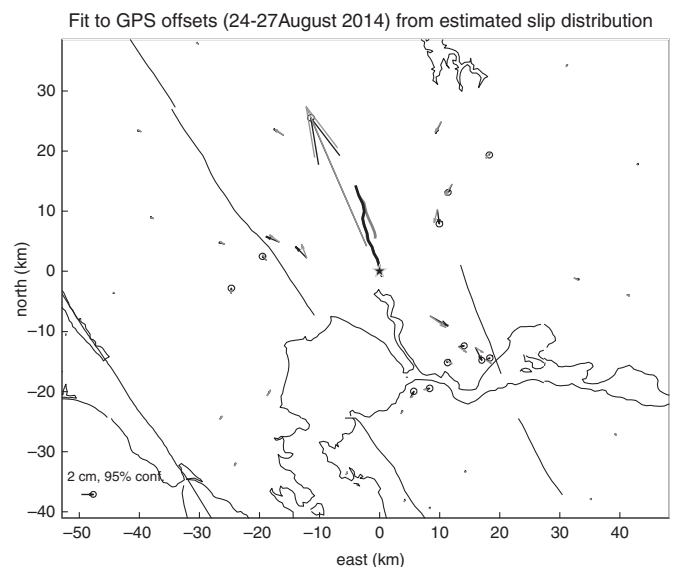
(1978) noted that the April 1906 San Francisco earthquake was preceded by an above average rainy season and a month of exceptionally heavy rainfall in March, yet those authors found no reports of ground failures in 1906 in the Napa Valley.

The relative scarcity of ground failures during the 2014 South Napa earthquake may partly reflect the low groundwater table resulting from the occurrence of the earthquake near the end of the dry season and a three-year-long drought. The South Napa earthquake occurred near the end of the summer dry season, with no appreciable rain being measured in Napa for nearly 4 months (i.e., since April 25; [Napa County University of California Cooperative Extension, 2015](#)). Total rainfalls in Napa during the two rainy seasons prior to the earthquake were 70% and 53% of average, respectively ([Napa](#)



▲ **Figure 10.** Offsets from field measurements of the rupture trace (24 August 2014). Circles mark the observations, and diamonds shown the inferred slip from inversion for the corresponding locations along the model fault surface trace. Approximate uncertainties for measured offsets are less than or equal to 5 cm.

[County University of California Cooperative Extension, 2015](#)). The USGS stream gage record for the Napa River shows that in the month before and on the day of the earthquake, the stream levels were lower than since before January 2008 and



▲ **Figure 11.** GPS offsets for 24–27 August 2014 (inclusive of coseismic slip). Black arrows show the estimated offset from the position time series, and gray arrows show predicted offset from the slip model shown in Figure 9b. The dark gray curve shows a surface trace of the model fault, and the light gray curve shows the location of the mapped eastern strand of the surface rupture (not included in model).



▲ **Figure 12.** Left-stepping en echelon fractures characteristic of right-lateral fault displacement at the ground surface. The total fault slip measured near this location was 40–46 cm. The photograph was taken by Dan Ponti on the main rupture strand near Buhman Road on the day following the earthquake.

that stream discharge rates were at low levels ($1.6 \text{ ft}^3/\text{s}$) (USGS, 2015).

Although we have not systematically reviewed records of groundwater levels in Napa Valley, a preliminary review of data from several selected water wells in the Napa area (California Department of Water Resources, 2015) indicates that the seasonal variation in the depth to the top of ground water in Napa Valley is in the 2–12 m range (6–40 ft) and that depths to the tops of groundwater tables approach their lowest point at the end of August. One water well, located in the center of Napa Valley about 4.3 km north of downtown and 0.6 km west of Napa River, shows that groundwater levels have dropped about 1.4 m since 2006; and, at the time of the South Napa earthquake, the water level in this well was at depth of 13.4 m. Many practitioners consider triggering of liquefaction at depths more than about 13–16 m to be uncommon; and, should it occur, it is unlikely to deform the ground surface. We believe that the low groundwater table in Napa Valley at the time of the earthquake reduced the saturation of the young sands and sandy deposits and inhibited liquefaction.

We also considered the liquefaction susceptibility of deposits in Napa Valley when saturated. Jennifer Thornburg of the CGS (verbal comm., 2015) reviewed borehole logs from Napa Valley on file at CGS and identified few liquefiable deposits. She found the young deposits are typically too fine grained to be liquefiable. We speculate that the low gradients of streams in the center of Napa Valley and the potential absence of suitable coarser-grained materials sourced from the surrounding hills (volcanic bedrock in the hills tend to weather to finer-grained material) may contribute to the absence of deposits prone to liquefaction.

Finally, as noted by Seed *et al.* (1983) from a liquefaction viewpoint, “the main difference between different magnitude

events is the number of cycles of stress which they induce.” The South Napa earthquake produced only 2–4 stress cycles in the strong ground motions in downtown Napa (station N016), fewer than expected for an M_w 6 earthquake (5–6 cycles).

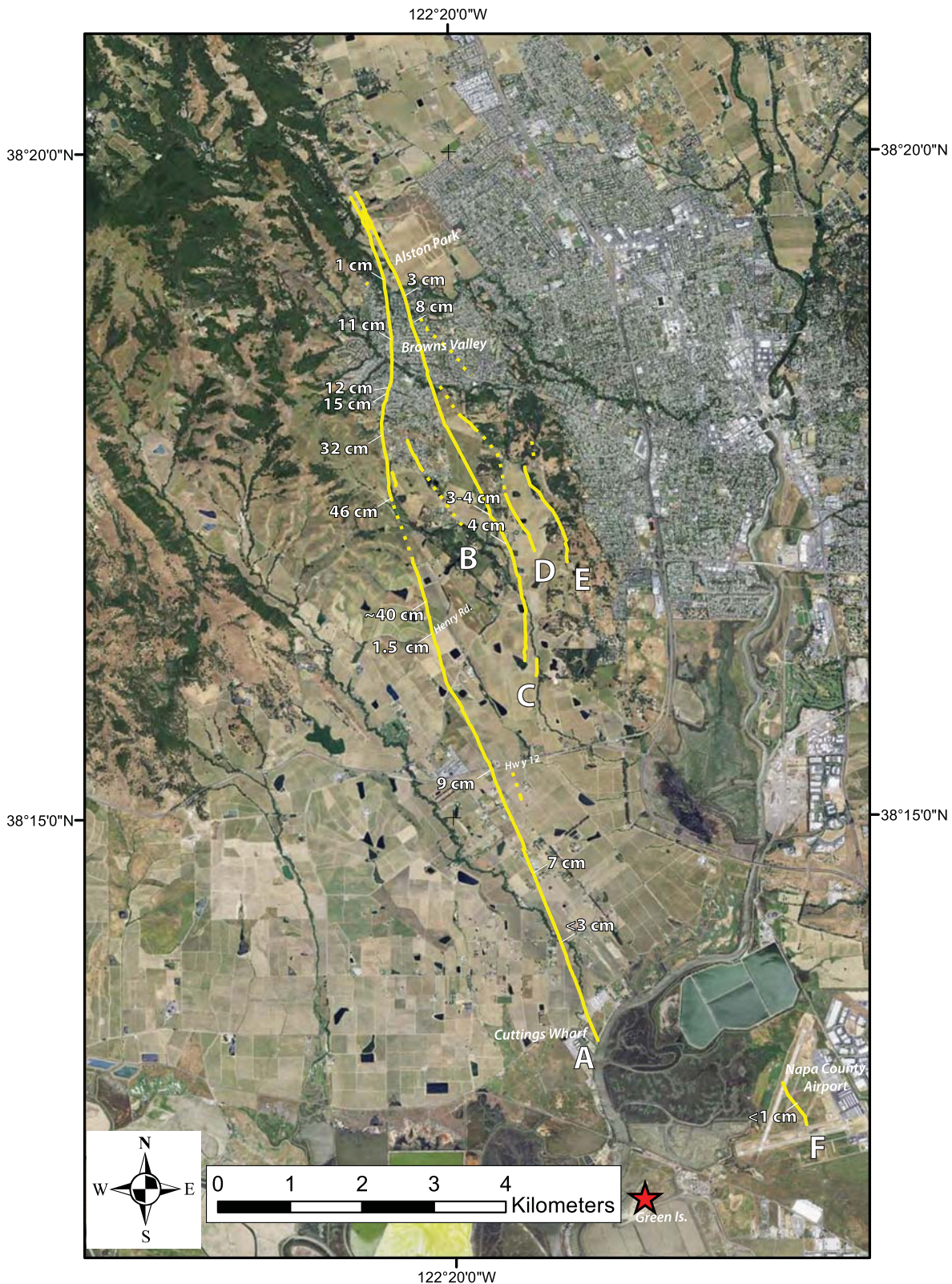
SITE RESPONSE

Comparison of the mapped red- and yellow-tagged structures with the mapped surface geology in Figure 1 indicates that the majority of these damaged buildings were built on three main soil types (Witter *et al.*, 2006): historic alluvial deposits from the Napa River and Napa Creek (Qhc), Holocene alluvial deposits (Qha), and Holocene fan deposits (Qhf2). There is a suggestion in Figure 1 that the boundary between Latest Pleistocene and Holocene fan deposits marks the northern boundary of the red- and yellow-tags in northern Napa, apart from tags in the older fan deposits associated with mobile home parks. Boatwright *et al.* (2015) notes a correlation of the locations of these damaged structures with the isocontours of the thickness of the Napa basin. It seems likely that the deposits in the Napa basin amplified the ground motions in the city of Napa and contributed to the damage there.

Temporary seismic stations were deployed by the USGS in the Napa region to record aftershocks (Fig. 1). A valley-crossing, east-trending deployment of six stations was made near the northern limit of the surface rupture. A north-trending deployment of seven stations was made along the trend of the Napa Valley. Five sites were deployed in downtown Napa to investigate the spatial variability of the strong shaking at a finer scale. The California State University–East Bay deployed three stations in Napa that complemented these arrays (not shown in Fig. 1). Finally, dense arrays of instruments were deployed across three separate fault strands to record fault-zone-guided waves to investigate the connectivity of the fault strands (Catchings *et al.*, 2014). A comparison of the aftershock recordings from five stations in downtown Napa reveals little variation in site response over a distance of a kilometer (Hudnut *et al.*, 2014).

DISCUSSION

The M_w 6.0 South Napa earthquake, the largest in the San Francisco Bay area in 25 years, occurred on the West Napa fault system, a known but relatively minor dextral strike-slip fault lying between the larger Rodgers Creek and Green Valley faults. The earthquake is a reminder not only that magnitude M_w 6.0 earthquake can occur on relatively minor fault systems throughout the Bay area and California in general and that often these minor fault systems have not been well characterized. Another lesson is that earthquakes of this magnitude can cause substantial ground motions resulting in significant damage to buildings that were not built to current building code standards. Fortunately, the EERI field team survey reported that buildings that had been retrofit generally fared better than those that had not (EERI, 2014). This point is well illustrated by the recording made by a USGS NetQuakes seismometer in



▲ **Figure 13.** Locations of the traces of tectonic surface faulting (yellow lines) produced by the 24 August 2014 South Napa earthquake from [Hudnut *et al.* \(2014\)](#). Right-lateral surface displacements, measureable in the field, were observed along traces labeled A–F. Solid lines indicate regions where surface faulting was relatively continuous. Dotted lines indicate regions where surface faulting was discontinuous, diffuse, or had negligible offset. Numbers show the earliest measurements of the maximum measured right-lateral offset at selected sites, rounded to the nearest centimeter; the measurements were made within two days of the earthquake, but probably include both coseismic slip and afterslip south of Henry Road. The red star is the location of the earthquake epicenter.

Table 1
Comparison of Seismological and Surface-Faulting Parameters for $\sim M_w$ 6 Strike-Slip Earthquakes in California since 1948

Event (Year)	Magnitude (M_w)*	Focal Depth D (km) [†]	Coseismic Surface Rupture Length (km) [‡]	Coseismic D_{max} at Surface (cm) [§]	Creep Prior to Event	Surface Afterslip (cm) [⊗]	Notes
Desert Hot Springs (1948)	6.0	6.0	0	0	No	nr	M_w and D (Felzer, 2013). Richter <i>et al.</i> (1958) report no surface rupture; 18 km aftershock zone.
Galway Lake (1975)	5.0 M_L	5.8	6.8	1.5	No	nr	M_L and D (Felzer, 2013). Surface offset data from Hill and Beeby (1977).
Parkfield (1966)	6.0	8.6	0 (SA) 10 (SWFZ)	0 (SA) 6.6 (SWFZ)	Yes	31 (SA)	M_w and D (Ellsworth, 1990). San Andreas creeping at 28 mm/yr. Afterslip along 44 km of main San Andreas (SA) Coseismic slip on southwest fracture zone (SWFZ). Surface offset data from Lienkaemper and Prescott (1989).
Homestead Valley (1979)	4.8 M_L 5.5 4.5 M_L 4.8 M_L	8.3 9.3 8.9 2.0	3.25 (HV) 1.5 (JV)	11 1	No	nr	M_w , M_L and D (Felzer, 2013). Earthquake swarm with rupture along Homestead Valley (HV) and Johnson Valley (JV) faults; both reruptured during 1992 M_w 7.2 Landers event. Surface offset data from Hill <i>et al.</i> (1980).
Coyote Lake (1979)	5.9	8.95	0	0	Yes	0.5	M_w and D (Oppenheimer <i>et al.</i> , 1990); 14 km rupture length at depth. Discontinuous surface cracking for 14.4 km is likely afterslip. Surface observations from Armstrong (1979).
Greenville (1980)	5.8	14.8	4–6	≥ 1	Yes	≥ 1	M_w and D (Ellsworth, 1990). Pre-event creep at 1–2 mm/yr (Lienkaemper <i>et al.</i> , 2013). Total surface slip (coseismic + afterslip) was 2.5 cm (Bonilla <i>et al.</i> , 1980). Concurrent rupture of conjugate Las Positias fault.
Morgan Hill (1984)	6.2	8.4	0	0	Yes	nr	M_w and D (Oppenheimer <i>et al.</i> , 1990). 25 km rupture length at depth (between 4 and 10 km). No unequivocal coseismic surface rupture (Harms <i>et al.</i> , 1987).

*Magnitudes are M_w unless noted as M_L . Data are from the Uniform California Earthquake Rupture Forecast Version 3 (UCERF 3) seismicity catalog (Felzer, 2013) unless otherwise noted.

[†]Focal depth D (km) source is UCERF 3 seismicity catalog (Felzer, 2013) unless otherwise noted.

[‡]Coseismic surface rupture length (km) is the reported length of rupture at the surface at time of event and is distinct from afterslip. Where multiple fault traces occurred, the length listed is for the longest trace.

[§]Coseismic D_{max} is the reported maximum coseismic surface displacement and does not include afterslip.

[⊗]nr, not reported.

(Continued next page.)

Table 1 (continued)

Comparison of Seismological and Surface-Faulting Parameters for $\sim M_w$ 6 Strike-Slip Earthquakes in California since 1948

Event (Year)	Magnitude (M_w)*	Focal Depth D (km) [†]	Coseismic Surface Rupture Length (km) [‡]	Coseismic D_{max} at Surface (cm) [§]	Creep Prior to Event	Surface Afterslip (cm) [⊗]	Notes
North Palm Springs (1986)	6.02	10.4	9	< 0.1	No	nr	M_w and D (Felzer, 2013). Discontinuous, en echelon, left-stepping fractures for 9 km along surface trace Banning strand of SA. Offset data from Sharp <i>et al.</i> (1986), who refer to these as trace fractures and interpret them as incipient faulting.
Elmore Ranch (1987)	6.04	10.8	10	20	No	nr	M_w and D (Felzer, 2013). Slip distributed on six traces across 8.5 km wide zone. Longest is 10 km (Elmore Ranch fault). Cumulative surface D_{max} for all traces is 20 cm, average ~ 10 cm surface offset data from Hudnut <i>et al.</i> (1989).
Joshua Tree (1992)	6.15	12.3	0	0	No	nr	M_w and D (Felzer, 2013). 1.5 km discontinuous, triggered slip on East Wide Canyon fault (Rymer, 2000).
Parkfield (2004)	6.0	7.9	0 (SA) 8 (SWFZ)	<0.2 (SA) 6.6 (SWFZ)	Yes	13–36 SA	M_w and D (USGS). No measurable coseismic rupture on main San Andreas (SA) but followed by 32 km of discontinuous afterslip varying from 13 to 36 cm. Coseismic rupture on southwest fracture zone (SWFZ). Offset data from Langbein <i>et al.</i> (2006) and Lienkaemper <i>et al.</i> (2006).
South Napa (2014)	6.0	10.7	≥ 12.5	≥ 60	No	≥ 35	M_w and D (USGS). Rupture involved five fault traces; some may be triggered. Longest (western) is a minimum of 12.5 km. Afterslip on west trace, primarily along southern 8.5 km; value listed is after 60 days with afterslip ongoing. Coseismic D_{max} combines strands A (46 cm), C (8 cm), and E (6 cm) traces.

*Magnitudes are M_w unless noted as M_L . Data are from the Uniform California Earthquake Rupture Forecast Version 3 (UCERF 3) seismicity catalog (Felzer, 2013) unless otherwise noted.

[†]Focal depth D (km) source is UCERF 3 seismicity catalog (Felzer, 2013) unless otherwise noted.

[‡]Coseismic surface rupture length (km) is the reported length of rupture at the surface at time of event and is distinct from afterslip. Where multiple fault traces occurred, the length listed is for the longest trace.

[§]Coseismic D_{max} is the reported maximum coseismic surface displacement and does not include afterslip.

[⊗]nr, not reported.

downtown Napa of PGA of 61%g at the foundation level of a masonry building that had been retrofit and suffered essentially no damage (Erol Kalkan, written comm., 2014).

The earthquake produced an unusual amount of surface rupture, triggered slip, and afterslip for its magnitude. Although using UAVSAR and other SAR imagery to guide the field mapping of surface rupture and deformation was not novel, the field mapping and imagery were unusually well integrated for this earthquake. The monitoring of afterslip with repeat photography, alignment arrays, mobile LiDAR, repeat SAR imagery, and GPS is ongoing but represents a standard of practice that should be used following future surface-rupturing earthquakes.

The focal mechanism and mapping of the surface rupture helped to document the southwest-dipping fault plane of the mainshock. The aftershocks also appear to define a northeast-dipping fault plane, of more moderate dip, that intersects the mainshock fault plane at a depth of about 9–10 km. The intersection of these faults causes a well-resolved south-dipping streak of seismicity and may give clues for the origin of other linear seismicity streaks observed elsewhere.

Finally, we note the South Napa earthquake was well recorded by seismometers and accelerometers and produced a useful set of strong-motion data in the near-field that have engineering implications. These recordings are a testament to the steady investment in upgrading seismic instrumentation and the benefits that are derived from this investment, including EEW.

DATA AND RESOURCES

Data from ShakeMap are available for download at <http://earthquake.usgs.gov/earthquakes/eventpage/nc72282711#shakemap> (last accessed February 2015). V_{S30} values at each station are taken from the Next Generation Attenuation-West 2 (NGA-West 2) database (http://peer.berkeley.edu/assets/NGA_West2_supporting_data_for_flatfile.zip; last accessed February 2015) or, if the station is not in the NGA-West 2 database, from the grid.xml file available with the ShakeMap (<http://comcat.cr.usgs.gov/product/shakemap/nc72282711/nc/1411172037430/download/grid.xml>; last accessed February 2015). Recorded strong-motion data are available at the Center for Engineering Strong-Motion Data (http://strongmotioncenter.org/cgi-bin/CESMD/iqr_dist_DM2.pl?iqrID=SouthNapa_24Aug2014_72282711&SFlag=0&Flag=2; last accessed February 2015). The moment tensor solution is from http://www.ncedc.org/mt/nc72282711_MT.html (last accessed February 2015). Global Positioning System data are available from <http://earthquake.usgs.gov/monitoring/gps/SFBayArea/> (last accessed February 2015). ✉

ACKNOWLEDGMENTS

We would like to acknowledge financial support from the Earthquake Hazards Program of the U.S. Geological Survey (USGS), the California Geological Survey (CGS), and the Federal Emergency Management Agency (FEMA). Anne Rosinski, CGS, coordinated the CGS Earthquake Clearinghouse at Napa. Mike Oskin at University of California–Davis and his

students conducted the initial mapping used to help define the surface rupture. We acknowledge with gratitude the contributions of the many individuals who assisted following the earthquake. For permanent network operations: Dave Croker, Lynn Dietz, Walt Jungblut, Fred Klein, Will Kohler, John Krueger, John Lee, Jim Luetgert, Harold Macbeth, Jonah Merritt, David H. Oppenheimer, Salvador Robles, Jim Smith, Nick Stein, Chris Stephens, Robert Summers, Roy Tam, and Jack Tomey. For assistance in field mapping: Mike Bennett, Steve B. Delong, Suzanne Hecker, Thomas L. Holzer, Alexandra Pickering, John Tinsley, Nikita Avdievitch, Carol Prentice, Carla Rosa, and Robert Sickler. For geodetic monitoring: Chris Guillemot, John Langbein, Eleyne Phillips, Jim Sutton, Jerry Svarc, and Chuck Wicks. For the aftershock deployment: Rufus Catchings, Coyn Criley, Shane Detweiler, Russell Sell, Jemille Erdem, Lind Gee, John Hamilton, Alena Leeds, Steve Ploetz, Steve Roberts, Joe Svitek, and Dave Wilson. Bill Ellsworth, Robert Graves, Tom Parsons, Ross Stein, and an anonymous journal reviewer reviewed earlier drafts of this paper.

This project in part was carried out using COSMO–SkyMed products, Agencia Spaziale Italiana (ASI), delivered under the ASI license provided under the Caltech/JPL-ASI/CIDOT CaliMap project. The continuous Global Positioning System data used in this study were recorded by instruments of the Plate Boundary Observatory (PBO; <http://pbo.unavco.org/>; last accessed February 2015) and the Bay Area Regional Deformation network (<http://seismo.berkeley.edu/bard/>; last accessed February 2015). The PBO is operated by UNAVCO for EarthScope (www.earthscope.org; last accessed February 2015) and supported by the National Science Foundation (Grant Numbers EAR-0350028 and EAR-0732947). Any use of trade, firm, or product names is for descriptive purposes only and does not imply endorsement by the U.S. Government.

REFERENCES

- Abrahamson, N., W. Silva, and R. Kamai (2014). Summary of the ASK14 ground-motion relation for active crustal regions, *Earthq. Spectra* **30**, 1025–1055.
- Armstrong, C. F. (1979). Coyote Lake earthquake, August 6, 1979, California, *Geology* **32**, 248–251.
- Bakun, W. H. (1999). Seismic activity in the San Francisco Bay region, *Bull. Seismol. Soc. Am.* **89**, 764–784.
- Baltay, A. S., and J. Boatwright (2015). Ground motion observations of the 2014 South Napa earthquake, *Seismol. Res. Lett.* **86**, no. 2A, doi: [10.1785/0220140232](https://doi.org/10.1785/0220140232).
- Baltay, A. S., and T. C. Hanks (2014). Understanding the magnitude dependence of PGA and PGV in NGA-West2 data, *Bull. Seismol. Soc. Am.* **104**, no. 6, 2851, doi: [10.1785/0120130283](https://doi.org/10.1785/0120130283).
- Boatwright, J., J. L. Blair, B. T. Aagaard, and K. Wallis (2015). The distribution of red and yellow tags in the City of Napa, *Seismol. Res. Lett.* **86**, no. 2A, doi: [10.1785/0220140234](https://doi.org/10.1785/0220140234).
- Bonilla, M. G., J. J. Lienkaemper, and J. C. Tinsley (1980). Surface faulting near Livermore, California, associated with the January 1980 earthquakes, *U.S. Geol. Surv. Open-File Rept.* 80-523, 27 pp.
- Boore, D. M., J. P. Stewart, E. Seyhan, and G. M. Atkinson (2014). NGA-West2 equations for predicting PGA, PGV, and 5%-damped PSA for shallow crustal earthquakes, *Earthq. Spectra* **30**, 1057–1085, doi: [10.1193/070113EQS184M](https://doi.org/10.1193/070113EQS184M).

- Brooks, B., K. Hudnut, C. Glennie, and T. Ericksen (2014). Near-field deformation associated with the M 6.0 South Napa earthquake surface rupture, presented at *2014 Fall Meeting, American Geophysical Union*, San Francisco, California, 15–19 December 2014, Abstract S33F-4900.
- Brossy, C., K. Kelson, and M. Ticci (2010). Digital compilation of data for the Contra Costa shear zone for the northern California Quaternary fault map database: Collaborative research with William Lettiss & Associates, Inc. and the U.S. Geological Survey, *Final Technical Rept.*, Award No. 07HQGR0063, 4 figures, 13 pp., <http://earthquake.usgs.gov/research/external/reports/07HQGR0063.pdf> (last accessed February 2015).
- California Department of Water Resources (2015). Groundwater level data reports, *Report Groundwater Level Data by Basin*, available at <http://www.water.ca.gov/waterdatalibrary/groundwater/hydrographs/index.cfm> (last accessed February 2015).
- Campbell, K. W., and Y. Bozorgnia (2014). NGA-West2 ground motion model for the average horizontal components of PGA, PGV, and 5%-damped linear acceleration response spectra, *Earthq. Spectra* **30**, 1087–1115, doi: [10.1193/062913EQS175M](https://doi.org/10.1193/062913EQS175M).
- Catchings, R., M. Goldman, G. Slad, C. Criley, J. Chan, R. Fay, W. Fay, and J. Svitek (2014). Continuity of the West Napa fault zone inferred from aftershock recordings on fault-crossing arrays, *2014 Fall Meeting*, San Francisco, California, 15–19 December 2014, Abstract #S31G-08.
- Chiou, B. S. J., and R. R. Youngs (2014). Update of the Chiou and Youngs NGA model for the average horizontal component of peak ground motion and response spectra, *Earthq. Spectra* **30**, 1117–1153, doi: [10.1193/072813EQS219M](https://doi.org/10.1193/072813EQS219M).
- d'Alessio, M. A., I. A. Johanson, R. Bürgmann, D. A. Schmidt, and M. H. Murray (2005). Slicing up the San Francisco Bay area: Block kinematics and fault slip rates from GPS-derived surface velocities, *J. Geophys. Res.* **110**, no. B06403, doi: [10.1029/2004JB003496](https://doi.org/10.1029/2004JB003496).
- Earthquake Engineering Research Institute (EERI) (2014). M 6.0 South Napa earthquake of August 24, 2014, *EERI Special Earthquake Report*, October 2014, 27 pp., <http://www.eqclearinghouse.org/2014-08-24-south-napa/preliminary-reports/> (last accessed February 2015).
- Ellsworth, W. L. (1990). Earthquake history, 1769–1989, in *The San Andreas Fault System, California*, Chapter 6, R. E. Wallace (Editor), United States Government Printing Office, Washington, *U.S. Geol. Surv. Prof. Pap.* 1515, 152–187.
- Felzer, K. R. (2013). Appendix K. The UCERF3 earthquake catalog, *U.S. Geol. Surv. Open-File Rept. 2013–1165, California Geol. Surv. Special Rept.* 228, and Southern California Earthquake Center Publication 1792.
- Field, E. H., G. P. Biasi, P. Bird, T. E. Dawson, K. R. Felzer, D. D. Jackson, K. M. Johnson, T. H. Jordan, C. Madden, A. J. Michael, et al. (2013). Uniform California earthquake rupture forecast, version 3 (UCERF3)—The time-independent model, *U.S. Geol. Surv. Open-File Rept. 2013–1165, California Geol. Surv. Special Rept.* 228, and Southern California Earthquake Center Publication 1792, 97 pp., <http://pubs.usgs.gov/of/2013/1165/> (last accessed February 2015).
- Geotechnical Extreme Events Reconnaissance [GEER] (2014). August 24, 2014 South Napa, California earthquake, *GEER Association Report No. GEER-037*, Section G, http://www.geerassociation.org/GEER_Post%20EQ%20Reports/SouthNapa_2014/index.html (last accessed February 2015).
- Given, D. D., E. S. Cochran, T. Heaton, E. Hauksson, R. Allen, P. Hellweg, J. Vidale, and P. Bodin (2014). Technical implementation plan for the ShakeAlert production system: An earthquake early warning system for the West Coast of the United States, *U.S. Geol. Surv. Open-File Rept. 2014-1097*, 31 pp.
- Graizer, V., and E. Kalkan (2015). Update of the Graizer–Kalkan ground-motion prediction equations for shallow crustal continental earthquakes, *U.S. Geol. Surv. Open-File Rept. 2015-1009*, 98 pp.
- Graymer, R. W., D. L. Jones, and E. E. Brabb (2002). Geologic map and map database of northeastern San Francisco Bay region, California, *U.S. Geol. Surv. Misc. Field Studies Map MF-2403*, version 1.0, scale 1:100,000.
- Hardebeck, J. L., and D. R. Shelly (2014). Aftershocks of the 2014 M 6 South Napa earthquake: Detection, location, and focal mechanisms, presented at *2014 Fall Meeting, American Geophysical Union*, San Francisco, California, 15–19 December 2014, Abstract S33F-4927.
- Hardebeck, J. L., A. J. Michael, and T. M. Brocher (2007). Seismic velocity structure and seismotectonics of the eastern San Francisco Bay region, California, *Bull. Seismol. Soc. Am.* **97**, 826–842.
- Harms, K. K., M. M. Clark, M. J. Rymer, M. G. Bonilla, E. L. Harp, D. G. Herd, K. R. Lajoie, J. J. Lienkaemper, S. A. Mathieson, J. A. Perkins, et al. (1987). The search for surface faulting, in *The Morgan Hill, California earthquake of April 2, 1984*, Hoose, S. N. (Editor), Chapter 7, *U.S. Geol. Surv. Bull.* 1639, 61–68.
- Hill, R. L., and D. J. Beeby (1977). Surface faulting associated with the 5.2 magnitude Galway Lake earthquake of May 31, 1975: Mojave Desert, San Bernardino County, California, *Geol. Soc. Am. Bull.* **88**, 1378–1384.
- Hill, R. L., J. A. Treiman, J. W. Given, J. C. Pechman, J. R. McMillan, and J. E. Ebel (1980). Geologic study of the Homestead Valley earthquake swarm of March 15, 1979, California, *Geology* **33**, 60–67.
- Hough, S. E. (2014). Where was the 1898 Mare Island earthquake? Insights from the 2014 South Napa earthquake, *2014 Fall Meeting, American Geophysical Union*, San Francisco, California, 15–19 December 2014, Abstract #S44D-03.
- Hudnut, K. W., T. M. Brocher, C. S. Prentice, J. Boatwright, B. A. Brooks, B. T. Aagaard, J. L. Blair, J. Fletcher, J. E. Erdem, and C. W. Wicks, et al. (2014). Key recovery factors for the August 24, 2014, South Napa earthquake, *U.S. Geol. Surv. Open-File Rept. 2014–1249*, 51 pp., doi: [10.3133/ofr20141249](https://doi.org/10.3133/ofr20141249).
- Hudnut, K. W., L. Seeber, and T. Rockwell (1989). Slip on the Elmore Ranch fault during the past 330 years and it's relation to slip on the Superstition Hills fault, *Bull. Seismol. Soc. Am.* **79**, 330–341.
- Jennings, C. W. (1994). Fault activity map of California and adjacent areas with locations and ages of recent volcanic eruptions, *California Geol. Surv., Geologic Data Map No. 6*, scale 1:750,000, Department of Conservation.
- Johanson, I. A., and R. Bürgmann (2010). Coseismic and postseismic slip from the 2003 San Simeon earthquake and their effects on back-thrust slip and the 2004 Parkfield earthquake, *J. Geophys. Res.* **115**, no. B07411, doi: [10.1029/2009JB006599](https://doi.org/10.1029/2009JB006599).
- Kelson, K. I., J. N. Baldwin, J. R. Unruh, and W. R. Lettiss (2004). Coastal marine terraces define Late Quaternary fault activity and deformation within northern East Bay hills, San Francisco Bay region, *Eos Trans. AGU* **85**, no. 47 (Fall Meet. Suppl.), Abstract T13C-1396.
- Kelson, K. I., J. R. Unruh, and J. N. Baldwin (2005). Late Quaternary deformation in the northeastern East Bay hills, San Francisco Bay region (abstracts with programs), *Geol. Soc. Am.* **37**, no. 4, 106, http://gsa.confex.com/gsa/2005CD/finalprogram/abstract_85559.htm (last accessed February 2015).
- Langbein, J. (2004). Noise in two-color electronic distance meter measurements revisited, *J. Geophys. Res.* **109**, no. B04406, doi: [10.1029/2003JB002819](https://doi.org/10.1029/2003JB002819).
- Langbein, J., J. R. Murray, and H. A. Snyder (2006). Coseismic and initial postseismic deformation from the 2004 Parkfield, California, earthquake observed by Global Positioning System, creepmeters, and borehole strainmeters, *Bull. Seismol. Soc. Am.* **96**, S304–S320.
- Langenheim, V. E., R. W. Graymer, and R. C. Jachens (2006). Geophysical setting of the 2000 M_L 5.2 Yountville, California, earthquake: Implications for seismic hazard in Napa Valley, California, *Bull. Seismol. Soc. Am.* **96**, 1192–1198.
- Lienkaemper, J. J., B. Baker, and F. S. McFarland (2006). Surface slip associated with the 2004 Parkfield, California, earthquake measured on alignment arrays, *Bull. Seismol. Soc. Am.* **96**, S239–S249, doi: [10.1785/0120050806](https://doi.org/10.1785/0120050806).

- Lienkaemper, J. J., G. R. Barry, F. E. Smith, and J. D. Mello (2013). The Greenville fault: preliminary estimates of its long-term creep rate and seismic potential, *Bull. Seismol. Soc. Am.* **103**, 2729–2738, doi:10.1785/0120120169.
- Lienkaemper, J. J., B. A. Brooks, S. B. DeLong, C. J. Domrose, and C. M. Rosa (2014). Surface slip associated with the 2014 South Napa, California earthquake measured on alignment arrays, *2014 Fall Meeting, American Geophysical Union*, San Francisco, California, 15–19 December 2014, Abstract #S33F-4898.
- Lienkaemper, J. J., and W. H. Prescott (1989). Historic surface slip along the San Andreas fault near Parkfield, California, *J. Geophys. Res.* **94**, 17,647–17,670.
- Minson, S. E., M. Simons, and J. L. Beck (2013). A Bayesian approach to finite fault earthquake modeling. I: Theory and synthetics, *Geophys. J. Int.* **194**, 1701–1726.
- Napa County University of California Cooperative Extension (2015). Carneros, Napa—Monthly Totals, <http://cenapa.ucanr.edu/about/weather/?weather=station&station=109> (last accessed February 2015).
- Ogata, Y. (1988). Statistical models for earthquake occurrences and residual analysis for point processes, *J. Am. Stat. Assoc.* **83**, 9–27.
- Oppenheimer, D. H., W. H. Bakun, and A. G. Lindh (1990). Slip partitioning of the Calaveras fault, California, and prospects for future earthquakes, *J. Geophys. Res.* **95**, 8483–8498.
- Ouillon, G., C. Ducorbier, and D. Sornette (2008). Automatic reconstruction of fault networks from seismicity catalogs, three-dimensional optimal anisotropic dynamic clustering, *J. Geophys. Res.* **113**, no. B01306, 15, doi: 10.1029/2007JB005032.
- Parsons, T., M. Segou, V. Sevilgen, K. Milner, E. Field, S. Toda, and R. S. Stein (2014). Stress-based aftershock forecasts made within 24 hours post-mainshock: Expected north San Francisco Bay area seismicity changes after the 2014 $M = 6.0$ West Napa earthquake, *Geophys. Res. Lett.* **41**, no. 24, 8792–8799, doi: 10.1002/2014GL062379.
- Ponti, D., T. Dawson, D. Schwartz, B. Brooks, S. DeLong, S. Hecker, K. Hudnut, K. Kelson, J. Lienkaemper, C. Prentice, C. Rosa, R. Rubin, G. Seitz, R. Sicker, and J. Wesling (2014). Surface fault rupture from the $M 6.0$ South Napa earthquake of August 24, 2014, presented at *2014 Fall Meeting, American Geophysical Union*, San Francisco, California, 15–19 December 2014, Abstract S33F-4901.
- Richter, C. F., C. R. Allen, and J. M. Nordquist (1958). The Desert Hot Springs earthquakes and their tectonic environment, *Bull. Seismol. Soc. Am.* **48**, 315–337.
- Rymer, M. J. (2000). Triggered surface slips in the Coachella Valley area associated with the 1992 Joshua Tree and Landers, California, earthquakes, *Bull. Seismol. Soc. Am.* **48**, 832–848.
- Seed, H. B., I. M. Idriss, and I. Arrango (1983). Evaluation of liquefaction potential using field performance data, *J. Geotech. Eng.* **109**, 458–482.
- Seyhan, E., and J. P. Stewart (2014). Semi-empirical nonlinear site amplification from NGA-West 2 data and simulations, *Earthq. Spectra* **30**, no. 3, 1241–1256, doi: 10.1193/063013EQS181M.
- Sharp, R. V., M. J. Rymer, and D. M. Morton (1986). Trace fractures on the Banning fault created in association with the 1986 North Palm Springs earthquake, *Bull. Seismol. Soc. Am.* **76**, no. 6, 1838–1843.
- Thurber, C., H. Zhang, F. Waldhauser, J. Hardebeck, A. Michael, and D. Eberhart-Phillips (2006). Three-dimensional compressional wave-speed model, earthquake relocations, and focal mechanisms for the Parkfield, California, region, *Bull. Seismol. Soc. Am.* **96**, S38–S49.
- Topozada, T. R., C. R. Real, and D. L. Parke (1981). Preparation of isoseismal maps and summaries of reported effects for pre-1900 California earthquakes, *California Div. Mines Geol. Open-File Rept. 81-11 SAC*, 182 pp.
- Trexler, C., A. Morelan, and M. Oskin (2014). Rapid mapping of surface rupture from the South Napa earthquake, presented at *2014 Fall Meeting, American Geophysical Union*, San Francisco, California, 15–19 December 2014, Abstract S31G-01.
- Unruh, J. R., and K. I. Kelson (2002a). Critical evaluation of the northern termination of the Calaveras fault, eastern San Francisco Bay area, California, unpublished *Final Technical Rept.* submitted to the U.S. Geological Survey National Earthquake Hazard Reduction Program, Award Number 00-HQ-GR-0082, dated July, 2002, 28 pp.
- Unruh, J. R., and K. I. Kelson (2002b). Critical evaluation of the northern termination of the Calaveras fault, eastern San Francisco Bay area, California (abstracts with programs), *Eos Trans. AGU* **83**, no. 47 (Fall Meet. Suppl.), Abstract T62F-04, 1300.
- U.S. Geological Survey (USGS) (2015). National Water Information System: Web Interface, *USGS Water Resources*, USGS 11458000 Napa River, Napa, California, http://waterdata.usgs.gov/ca/nwis/uv?site_no=11458000 (last accessed February 2015).
- Wald, L. (2012). Earthquake information products and tools from the Advanced National Seismic System (ANSS), *U.S. Geol. Surv. Fact Sheet 2006-3050* (revised September 2012), 2 pp.
- Wesling, J. R., and K. L. Hanson (2008). Mapping of the West Napa fault zone for input into the Northern California Quaternary Fault Database, *Final Technical Rept.*, U.S. Geol. Surv. External Award Number 05HQAG0002, 4 tables, 12 figures, 1 plate, 1 appendix, 34 pp., <http://earthquake.usgs.gov/research/external/reports/05HQAG0002.pdf> (last accessed February 2015).
- Witter, R. C., K. L. Knudsen, J. M. Sowers, C. M. Wentworth, R. D. Koehler, and C. E. Randolph (2006). Maps of Quaternary deposits and liquefaction susceptibility in the central San Francisco Bay region, California, *U.S. Geol. Surv. Open-File Rept. 2006-1037*, digital database by Wentworth, C. M., Brooks, S. K., and Gans, K. D., scale 1:24,000, <http://pubs.usgs.gov/of/2006/1037/> (last accessed February 2015).
- Youd, T. L., and S. N. Hoose (1978). Historic ground failures in northern California triggered by earthquakes, *U.S. Geol. Surv. Prof. Pap.* 993, U.S. Government Printing Office, Washington, iv, 177 pp.
- Zhang, H., and C. H. Thurber (2003). Double-difference tomography: The method and its application to the Hayward fault, California, *Bull. Seismol. Soc. Am.* **93**, 1875–1889.

Thomas M. Brocher
 Annemarie S. Baltay
 Jeanne L. Hardebeck
 Fred F. Pollitz
 Jessica R. Murray
 Andrea L. Llenos
 David P. Schwartz
 James Luke Blair
 Daniel J. Ponti
 James J. Lienkaemper
 John Boatwright
 Brad T. Aagaard
 Keith L. Knudsen
 Benjamin A. Brooks
 U.S. Geological Survey
 MS 977, 345 Middlefield Road
 Menlo Park, California 94025 U.S.A.
 brocher@usgs.gov

Victoria E. Langenbeim
 U.S. Geological Survey
 MS 989, 345 Middlefield Road
 Menlo Park, California 94025 U.S.A.

Timothy E. Dawson
 California Geological Survey
 MS 520, 345 Middlefield Road
 Menlo Park, California 94025 U.S.A.

*Kenneth W. Hudnut
Katherine M. Scharer
U.S. Geological Survey
525 South Wilson Avenue
Pasadena, California 91106 U.S.A.*

*David R. Shelly
U.S. Geological Survey
MS 910, 345 Middlefield Road
Menlo Park, California 94025 U.S.A.*

*Douglas S. Dreger
Richard M. Allen
Berkeley Seismological Laboratory
215 McCone Hall #4760
University of California, Berkeley
Berkeley, California 94720 U.S.A.*

*David J. Wald
U.S. Geological Survey
1711 Illinois Avenue
Golden, Colorado 80401 U.S.A.*

*William D. Barnhart¹
Department of Earth and Environmental Sciences
University of Iowa
Iowa City, Iowa 52242 U.S.A.*

Published Online 25 February 2015

¹ Also at: U.S. Geological Survey, 1711 Illinois Avenue, Golden, Colorado 80401 U.S.A.